

# Security-Constrained Inertial Response Provision in Distribution Grids

Georgios C. Kryonidis

*School of Electr. & Comput. Eng.*  
*Aristotle University of Thessaloniki*  
Thessaloniki, Greece  
kryonidi@ece.auth.gr

Charis S. Demoulias

*School of Electr. & Comput. Eng.*  
*Aristotle University of Thessaloniki*  
Thessaloniki, Greece  
chdimoul@auth.gr

**Abstract**—In this paper, an enhanced coordination strategy is proposed to facilitate the provision of virtual inertia (VI) in grid-connected distribution grids. Its distinct characteristic is the introduction of a proactive mechanism that determines the operating points of the main network elements, e.g., converter-interfaced renewable energy sources (CIRESs), to: (a) optimize the network operation in terms of reducing network losses and curtailment of green energy (b) meet the security and reliability standards under normal conditions and during VI provision. This is attained by solving an optimization problem where the operating set-points of CIRESs are calculated to meet the operating constraints both at normal conditions and during frequency events, while achieving the above optimization objectives. Time-domain and time-series simulations are conducted on the IEEE European low-voltage Test Feeder to evaluate the performance of the proposed approach.

**Index Terms**—Converter-interfaced renewable energy sources, distribution grids, tripping, virtual inertia, voltage regulation.

## I. INTRODUCTION

### A. Motivation and Background

Nowadays, the electrical grid is facing an unprecedented transition from fossil-fuel power plants to renewable energy sources (RES), revealing a series of technical problems that affect the secure and reliable operation [1]. Among them, inertia reduction can be regarded as one of the most important issues deteriorating the frequency stability of the system in terms of increased rate of change of frequency (RoCoF), reduced frequency nadir, etc. [2]. A promising solution to address the inertia scarcity is the active involvement of converter-interfaced RESs (CIRESs) by means of providing virtual inertia (VI) [3]. The validity of this approach has been already demonstrated in pilot installations and under real-field conditions [4].

### B. Relevant Literature

In the literature, the relevant research works can be classified into three main categories. The first category is devoted to the development and efficient integration of the VI functionality in CIRESs. An initial solution was proposed in [3] where an

analytic synchronous generator (SG) model is integrated into the CIRES control unit to imitate the dynamic properties of a real SG, i.e., inertial response, grid-forming capability, etc. Over the last decade, several variants of this solution have been proposed to address its inherent drawbacks related to the dynamic performance. Indicatively, a modified Andronov-Hopf oscillator is proposed in [5] to improve the CIRES self-synchronization with the grid. In [6], the application of the VI functionality is extended to grid-following CIRESs by introducing a frequency-sensitive voltage set-point at the dc link. Moreover, the conventional first-order filter-based approach for VI provision is replaced with a second-order low-pass filter in [7] to overcome potential stability issues in grid-following CIRESs. Finally, in [8] and [9], the VI constant is automatically adjusted with respect to the network frequency, thus offering a responsive and stable frequency support to the grid.

The second category focuses on improving the damping of CIRESs. Specifically, a proportional-integral controller is introduced in [10] that effectively decouples VI from primary frequency response. Additionally, a condition for a critically damped VI provision is presented. The authors in [11] adopt an alternative approach by moving the damping from the angle of the internal voltage as determined by the well-established swing equation to the corresponding voltage magnitude control loop. In [12], a virtual inductance control loop is introduced to provide additional damping support in highly resistive grids. Lastly, a comparative analysis is performed in [13] to assess the damping of various alternatives where the conventional swing equation is enhanced with additional control loops.

In the third category, the VI provision is examined from a system-wide perspective. In particular, the authors in [14] investigate the impact of various VI control schemes on the dynamic stability of a transmission system. Furthermore, a hierarchical control scheme is proposed in [15] that coordinates CIRESs and battery energy storage systems to improve system frequency response with reduced operational costs. In [16], a centralized, stability-constrained optimization control scheme is proposed to optimally determine the siting and sizing of VI sources. Finally, to improve the frequency stability under high CIRES penetration, an enhanced unit commitment strategy is proposed in [17] and [18] by considering fixed and variable

The work of G. C. Kryonidis is supported by the Research Committee of Aristotle University of Thessaloniki via a merit scholarship between 2024 and 2025.

The work of C. S. Demoulias has been funded by the European Union under the Horizon Europe project COCOON (GA 101120221).

frequency droop control schemes, respectively.

From the above, it is evident that the VI provision is a well-studied research topic at CIRES level that has been recently started to be explored at system level, emphasizing on the transmission system. As a result, the VI provision in distribution grids, where a significant part of CIRES share is connected, has been overlooked from these analyses.

### C. Contributions

Scope of this paper is to fill this gap by proposing a new security-constrained control scheme that facilitates the VI provision in unbalanced, grid-connected distribution grids. The primary objective is to avoid the tripping of CIRESs due to overvoltages during VI provision. This is attained by solving an optimization problem where the operating set-points of CIRESs are calculated to meet the operating constraints both at normal conditions and during frequency events, while maintaining minimum network losses and curtailment of green energy. The performance of the proposed method is assessed via time-series and time-domain simulations on the IEEE European low-voltage (LV) Test Feeder.

## II. PROPOSED CONTROL FRAMEWORK

### A. Main Concept

The recently amended IEEE 1547 Standard defines a series of technical requirements for the installation of CIRESs in distribution grids under steady-state and transient conditions [19]. Focusing on the latter, CIRESs shall trip within a given time period (clearing time) in case the voltage at the point of interconnection (POI) with the grid exceeds the predefined thresholds that are broader than the corresponding steady-state deviation limits of  $\pm 0.1$  p.u. Currently, the IEEE 1547 Std proposes a set of ranges for the voltage thresholds and the clearing time that trigger the CIRES tripping, leaving the exact determination of these settings to the discretion of the distribution system operator (DSO).

Based on the above, it is evident that these broader limits must be respected under any transient condition, including also a frequency event. To this end, a centralized, optimization-based control scheme is proposed that determines the operating set-points of CIRESs, i.e., the output active and reactive power, in order to: (a) minimize the network losses and the curtailment of green energy under steady-state conditions and (b) avoid CIRES tripping during a frequency event. Essentially, the short-term planning and operation of distribution grids is supplemented by a proactive mechanism to ensure that the voltage variations caused by the VI provision from CIRESs during a potential frequency event will remain within the foreseen thresholds.

In the next subsections, the CIRES model is firstly presented followed by the proposed centralized, optimization-based control scheme.

### B. CIRES Model

Assuming a CIRES connected at node  $i$ ,  $P_i^C$  and  $Q_i^C$  denote the active and reactive power outputs determined as follows:

$$P_i^C = P_i^{\text{set}} + \Delta P_i^{\text{vi}} \quad (1)$$

$$Q_i^C = Q_i^{\text{set}} \quad (2)$$

where  $P_i^{\text{set}}$  and  $Q_i^{\text{set}}$  are the active and reactive power set-points, respectively, determined by the centralized control scheme based on the analysis described in the next subsection. Note that these values remain constant till a new update is received by the central controller. Moreover,  $\Delta P_i^{\text{vi}}$  stands for the variation of the output active power due to the VI provision which is determined according to

$$\Delta P_i^{\text{vi}} = 2H \frac{S_i^r}{f_{\text{nom}}} \frac{df}{dt}. \quad (3)$$

Here,  $S_i^r$  and  $f_{\text{nom}}$  are the rated power of the CIRES connected at node  $i$  and the nominal grid frequency, respectively. Additionally,  $H$  is the inertia constant, while  $f$  denotes the grid frequency. It is worth mentioning that the damping term has been neglected in (3) to consider the ideal VI provision from CIRESs in the proposed control framework.

### C. Centralized Control Scheme

Under steady-state conditions, scope of the centralized control scheme is to use CIRESs as controllable active and reactive power sources to minimize the network losses and the curtailment of green energy, while also respecting the technical constraints of the grid, e.g., voltage limits. This control scheme is supplemented by a proactive mechanism aiming to avoid CIRES tripping during VI provision under a frequency event. Both targets are combined into a single optimization problem having the following objective:

$$\min \sum_{i \in N} P_i^{\text{curt}} + \Re(\bar{S}_{\text{loss}}) \quad (4)$$

where  $N$  and  $P_i^{\text{curt}}$  denote the set of network nodes and the curtailed active power of the CIRES connected at node  $i$ , respectively.  $\bar{S}_{\text{loss}}$  stands for the apparent power of the network losses which is calculated according to

$$\bar{S}_{\text{loss}} = \sum_{i \in N} \sum_{\substack{j \in N \\ j > i}} (\bar{\mathbf{V}}_i - \bar{\mathbf{V}}_j)^T [\bar{\mathbf{Y}}_{ij} (\bar{\mathbf{V}}_i - \bar{\mathbf{V}}_j)]^* \quad (5)$$

Here,  $\bar{\mathbf{V}}_i = [\bar{V}_i^a \ \bar{V}_i^b \ \bar{V}_i^c \ \bar{V}_i^n]^T$  is the vector containing the complex phase/neutral voltages of node  $i$ . Furthermore,  $\bar{\mathbf{Y}}_{ij}$  is the admittance matrix of the four-wire line connecting node  $i$  with node  $j$ .

Eqs. (6)-(10) describe the power flow model of a three-phase, four-wire unbalanced distribution grid. In particular, the nodal complex currents of node  $i$  ( $\bar{\mathbf{I}}_i = [\bar{I}_i^a \ \bar{I}_i^b \ \bar{I}_i^c \ \bar{I}_i^n]^T$ ) are calculated based on

$$\bar{\mathbf{I}}_i = \sum_{k \in N \setminus \{i\}} \bar{\mathbf{Y}}_{ki} \bar{\mathbf{V}}_k - \left( \sum_{k \in N \setminus \{i\}} \bar{\mathbf{Y}}_{ki} \right) \bar{\mathbf{V}}_i, \quad \forall i \in N. \quad (6)$$

At each node, Kirchhoff's first law shall be satisfied using (7).

$$\mathbf{1}^T \bar{\mathbf{I}}_i = \bar{I}_i^g, \quad \forall i \in N \quad (7)$$

$\bar{I}_i^g$  denotes the complex current flowing through the grounding resistance at node  $i$  ( $R_i^g$ ) and is given by

$$\bar{I}_i^g = \frac{\bar{V}_i^n}{R_i^g}, \quad \forall i \in N. \quad (8)$$

Finally, the relation between the net active ( $\mathbf{P}_i^{\text{net}} = [P_i^a \ P_i^b \ P_i^c]^T$ ) and reactive ( $\mathbf{Q}_i^{\text{net}} = [Q_i^a \ Q_i^b \ Q_i^c]^T$ ) power absorbed at each phase of node  $i$  and the corresponding nodal currents and voltages is provided below:

$$\mathbf{P}_i^{\text{net}} = \Re \left( [\bar{V}_i^{an} \bar{I}_i^{a*} \ \bar{V}_i^{bn} \bar{I}_i^{b*} \ \bar{V}_i^{cn} \bar{I}_i^{c*}]^T \right), \quad \forall i \in N \quad (9)$$

$$\mathbf{Q}_i^{\text{net}} = \Im \left( [\bar{V}_i^{an} \bar{I}_i^{a*} \ \bar{V}_i^{bn} \bar{I}_i^{b*} \ \bar{V}_i^{cn} \bar{I}_i^{c*}]^T \right), \quad \forall i \in N \quad (10)$$

where  $\bar{V}_i^{xn}$  denotes the voltage difference between phase  $x \in \{a, b, c\}$  and neutral  $n$  at node  $i$ . Moreover,  $\mathbf{P}_i^{\text{net}}$  and  $\mathbf{Q}_i^{\text{net}}$  are calculated according to (11) and (12), respectively.

$$\mathbf{P}_i^{\text{net}} = \mathbf{P}_i^L - \mathbf{P}_i^{\text{set}}, \quad \forall i \in N \quad (11)$$

$$\mathbf{Q}_i^{\text{net}} = \mathbf{Q}_i^L - \mathbf{Q}_i^{\text{set}}, \quad \forall i \in N \quad (12)$$

Here,  $\mathbf{P}_i^L$  and  $\mathbf{Q}_i^L$  are 3x1 vectors denoting the active and reactive power absorbed in each phase by the load connected to node  $i$ , while  $\mathbf{P}_i^{\text{set}}$  and  $\mathbf{Q}_i^{\text{set}}$  are the control variables of the optimization problem and refer to the corresponding active and reactive power of the CIRES connected at the same node. Note that in case of three-phase CIRESs, the overall active ( $P_i^{\text{set}}$ ) and reactive power ( $Q_i^{\text{set}}$ ) are equally split among the three phases. Furthermore, (13) and (14) are introduced to limit the control variables.

$$0 \leq P_i^{\text{set}} \leq P_i^{\text{mpp}}, \quad \forall i \in N \quad (13)$$

$$-Q_i^{\text{max}} \leq Q_i^{\text{set}} \leq Q_i^{\text{max}}, \quad \forall i \in N \quad (14)$$

$P_i^{\text{mpp}}$  stands for the maximum power point of the CIRES connected to node  $i$  for a given time instant, while  $Q_i^{\text{max}}$  denotes the corresponding maximum permissible reactive power limit that is equal to  $\sqrt{S_i^2 - P_i^{\text{set}^2}}$ . Based on the above, it is evident that  $P_i^{\text{curt}} = P_i^{\text{mpp}} - P_i^{\text{set}}$ .

Finally, (15) is used to maintain the positive-sequence network voltages within permissible limits as imposed by the IEEE 1547 Standard [19].

$$V_{\min}^{\text{ss}} \leq \|\bar{V}_i^{\text{pos}}\| \leq V_{\max}^{\text{ss}}, \quad \forall i \in N \quad (15)$$

$V_{\min}^{\text{ss}}$  and  $V_{\max}^{\text{ss}}$  are the minimum and maximum voltage limits under steady-state conditions that are set equal to 0.9 and 1.1 p.u., respectively.  $\bar{V}_i^{\text{pos}}$  is the positive-sequence voltage at node  $i$  that can be obtained using (16).

$$\bar{V}_i^{\text{pos}} = \frac{\bar{V}_i^{an}}{3} + \frac{\bar{V}_i^{bn}}{3} e^{i\frac{2\pi}{3}} + \frac{\bar{V}_i^{cn}}{3} e^{-i\frac{2\pi}{3}}, \quad \forall i \in N \quad (16)$$

The above mathematical formulation as described by (6)-(16) is used to model the steady-state operation of the distribution grid. This formulation is modified by introducing a new

set of equality and inequality constraints expressed by (17)-(18) that model the distribution grid under transient conditions, and specifically during a frequency event.

$$\mathbf{P}_i^{\text{net}} = \mathbf{P}_i^L - \mathbf{P}_i^{\text{set}} - \mathbf{1} \frac{\Delta P_i^{\text{vi}}}{3}, \quad \forall i \in N \quad (17)$$

$$V_{\min}^{\text{tc}} \leq \|\bar{V}_i^{\text{pos,tc}}\| \leq V_{\max}^{\text{tc}}, \quad \forall i \in N \quad (18)$$

Eq. (17) is introduced to consider the VI provision from CIRESs replacing (11). Moreover, (18) is used to model the CIRES voltage tripping thresholds replacing (15).  $\bar{V}_i^{\text{pos,tc}}$  stands for the positive-sequence voltage during transient conditions, while  $V_{\min}^{\text{tc}}$  and  $V_{\max}^{\text{tc}}$  denote the corresponding minimum and maximum permissible limits that are set equal to 0.88 and 1.12 p.u., respectively. Note that CIRES overloading during VI provision is allowed by the current formulation. The main reason lies on the small duration of the VI provision allowing the short-term overloading as analyzed in [20].

### III. SYSTEM UNDER STUDY

The validity of the proposed control framework is assessed on the 416 V European LV Test Feeder depicted in Fig. 1 [21]. Apart from the 55 single-phase loads of the initial configuration, 32 three-phase PVs are added. The location and the installed capacity of the PVs is provided in Table I, while the rated power factor is equal to 0.85, which corresponds to an oversizing factor of 1.176. Moreover, to facilitate the unbalance modeling of the examined distribution grid in terms of line impedance and grounding resistance determination, the modifications presented in [22] are adopted. Finally, all PVs are equipped with VI functionality having an inertia constant ( $H$ ) equal to 5 s.

### IV. NUMERICAL RESULTS

In this section, time-domain and time-series simulations are conducted to assess the short- and long-term performance, respectively, of the proposed control framework against the base case scenario where the proposed proactive mechanism remains deactivated. Specifically, in the base case scenario, the PV set-points are determined for each time instant by solving the optimization problem of (4)-(16), while in the proposed control framework, the optimization problem of (4)-(18) is solved. Both optimization problems are solved in GAMS using the CONOPT solver [23].

Regarding VI provision, a under-frequency event with a RoCoF equal to 1 Hz/s is assumed. During this event, the voltage of the slack bus is increased by 0.02 p.u. to consider the impact of the upstream medium-voltage grid.

#### A. Time-Domain Simulations

To avoid a prohibitive execution time, time-domain simulations are conducted on a reduced version of the IEEE European LV Test Feeder using PSIM software [24]. This part of the grid is denoted with green color in Fig. 1 and consists of 250 nodes. Table II contains the PV units and loads considered in these simulations. Additionally, the voltage at the slack bus is considered equal to 1.0675 p.u under steady-state conditions.

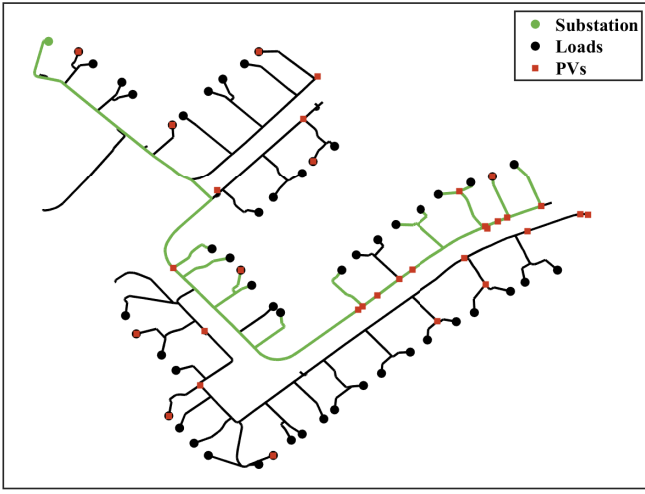


Fig. 1. Single-line diagram of the European LV Test Feeder. The part of grid denoted with green color is considered in the time-domain simulations.

TABLE I  
CONNECTION NODE AND RATED ACTIVE POWER OF PVs

kWp	Node											
5	70	166	234	247	248	388	403	447	453	482	556	
	567	580	588	619	651	763	785	845	861	869	884	
10	73	219	320	461	476	578	604	681	794	882		

Assuming that PVs can inject their rated power to the LV grid, the active and reactive power PV set-points for each examined scenario are calculated by solving the two distinct optimization problems presented above and are presented in Table III. Concerning the VI functionality, a grid-forming CIRESS with the control scheme proposed in [10] is considered.

The simulation results are presented in Fig. 2. In particular, the voltage magnitude and frequency of the slack bus is shown in Fig. 2a. The RMS value of the voltage magnitude measured by the most remote PV unit connected at node 619 is depicted in Fig. 2b. Finally, the output active/reactive power as well as the apparent power of an indicative PV unit connected at node 618 is presented in Figs. 2c and 2d, respectively. The frequency decrease starts at 0.5 s and ends at 1.5 s.

Considering the base case scenario, prior to the frequency event, the voltage at node 619 is kept constant and equal to the maximum permissible limit under steady-state conditions of 1.1 p.u., as verified in Fig. 2b. All PV units operate at rated active power, i.e., no curtailment is applied, as shown in Table III and Fig. 2c. It can be also observed that most of the PV units operate at non-unity power factor, mainly absorbing reactive power in order to partially compensate the voltage rise caused by the active power injection. During the frequency event, the output power of all the PV units is increased by 0.2 p.u. to provide VI as calculated by (3) and verified in Fig. 2c. This, in turn, leads to a voltage increase above the corresponding limit of 1.12 p.u., as shown in Fig. 2b. According to Fig. 2c, it can be seen that the reactive power output of the PV units remains almost unaffected during VI

TABLE II  
PVs AND LOADS CONSIDERED IN THE TIME-DOMAIN SIMULATIONS

PV Node	247	388	447	453	461	476	482	567	580	588	604	619	651	681
Load	19 20 21 22 29 31 33 34 35 36 37													

TABLE III  
ACTIVE AND REACTIVE POWER SET-POINTS IN P.U. OF PVs IN THE TIME-DOMAIN SIMULATIONS

PV Node	$P_{set}$		$Q_{set}$	
	Proposed	Base Case	Proposed	Base Case
247 388 447 453	0.8500	0.8500	-0.5268	-0.5268
461	0.8500	0.8500	-0.5268	-0.0138
476	0.8500	0.8500	-0.5268	0.0061
482	0.8500	0.8500	-0.5268	0.1155
567	0.7600	0.8500	-0.6499	-0.5268
580	0.7590	0.8500	-0.6511	-0.1898
588	0.7283	0.8500	-0.6853	-0.5268
604	0.6318	0.8500	-0.7751	-0.4785
619	0.5867	0.8500	-0.8098	-0.5268
651	0.7647	0.8500	-0.6444	0.0035
681	0.7590	0.8500	-0.6511	-0.1508

provision. A short-term overloading is also observed for the PV units operating close to the rated values prior to the frequency event, as shown in Fig. 2d.

On the contrary, the proposed control framework can effectively regulate the network voltages under both state-steady and transient conditions, i.e., during VI provision, as shown in Fig. 2b. This is attributed to the proactive mechanism that introduces a safety margin under steady-state conditions to ensure that even during a frequency event, the network voltages are kept within the permissible limits. This is evident in Fig. 2b, where the voltage prior the frequency event is kept far below the maximum permissible limit under steady-state conditions of 1.1 p.u. This is attained by activating active power curtailment and reactive power absorption in most of the PV units, as shown in Table III and Fig. 2c. Note that the short-term overloading of the PV units occurs in both examined scenarios. However, the proposed control framework ensures that the network voltages are within the permissible limits during VI provision, thus avoiding the potential tripping of CIRESSs.

### B. Long-term Evaluation

In this subsection, time-series simulations are conducted to assess the long-term performance of the examined scenarios. The simulation period is one day with a time resolution of 1 min. A sunny day is assumed for the PVs using the generation profiles of Fig. 3a. Indicative consumption profiles of the single-phase loads are presented in Figs. 3b, 3c, and 3d, which are obtained from [21]. Note that the power factor of the loads remains constant and equal to 0.95 inductive.

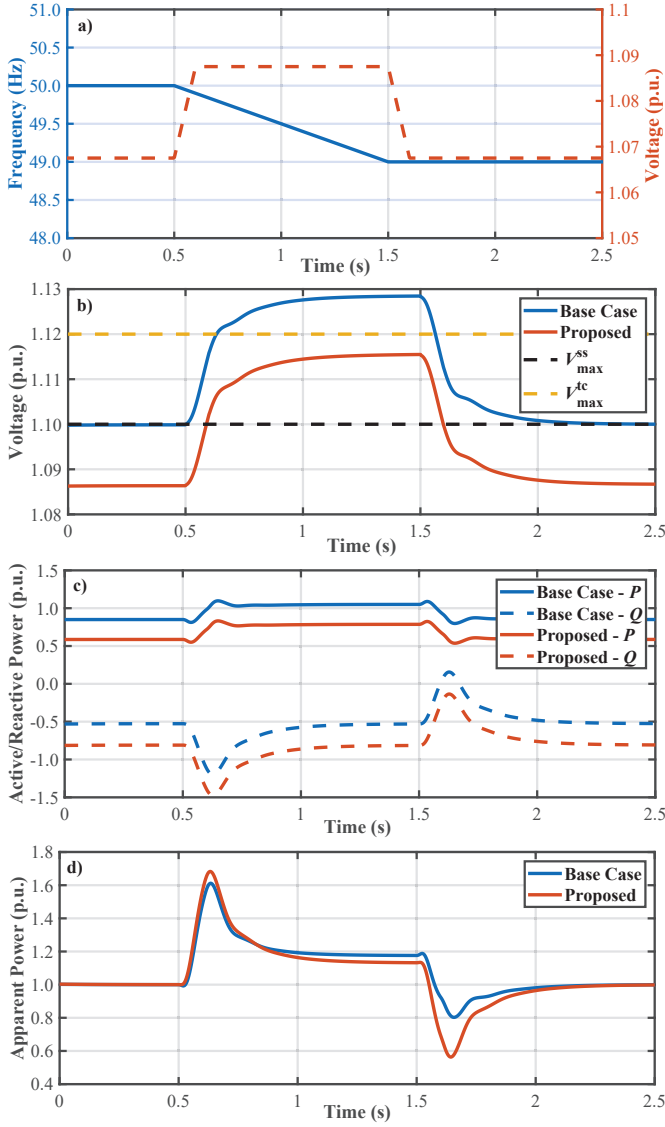


Fig. 2. Time-domain simulation results. a) Voltage magnitude and frequency imposed by the upstream grid, b) voltage magnitude at node 619, c) output active and reactive power of the PV connected at node 681 and d) the corresponding apparent power.

The corresponding results are depicted in Fig. 4 and Table IV. Specifically, the daily profiles of the network voltages under steady-state conditions for the base case scenario and the proposed control framework are presented in Figs. 4a and 4b, respectively. In Figs. 4c and 4d, the corresponding network voltages under transient conditions, i.e., during VI provision, are shown. The daily profile of the overall curtailed power and reactive power usage under steady-state conditions are illustrated in Figs. 4e and 4f. Finally, the network losses are presented in Fig. 4g, while aggregated daily values are shown in Table IV.

According to Figs. 4a and 4b, it can be observed that both examined scenarios can effectively regulate the network voltages under steady-state conditions within the permissible limits. Nevertheless, during VI provision, the base case scenario fails to keep the network voltages below the permissible limit

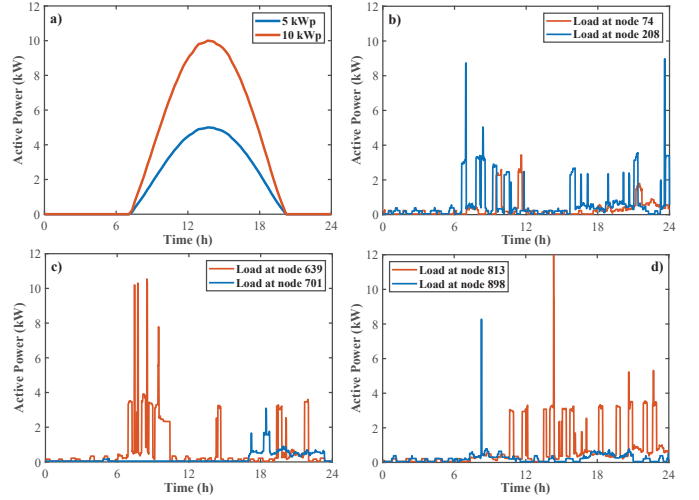


Fig. 3. Indicative daily profiles. a) Generation profiles, b), c), and d) consumption profiles.

TABLE IV  
DAILY ANALYSIS

	Curtailed Energy (kWh)	Reactive Energy (kVarh)	Energy Losses (kWh)
<b>Base Case</b>	0.00	408.78	54.43
<b>Proposed</b>	33.89	906.37	108.76

of 1.12 p.u., thus making the CIRES tripping unavoidable. Indicatively, at the time instant with the maximum CIRES generation, i.e., at 13:40, 19 out of 32 CIRESs will be disconnected since the corresponding POI voltages exceed 1.12 p.u., thus significantly reducing the VI provision. On the contrary, the proposed control framework overcomes this issue, as verified in Fig. 4b. However, by contrasting Figs. 4e and 4f, it is evident the proposed method leads to increased curtailed power and reactive power usage compared to the base case scenario. This is also evident in Table IV, where the daily curtailed energy and reactive energy are shown. Notably, the reactive energy is increased by 121.72 %, while curtailed energy does not exceed 2 % of the daily produced energy of 1662.9 kWh. It is worth mentioning that these values could be reduced if smaller VI contribution from CIRESs was considered, e.g., smaller inertia constant  $H$ . Similar conclusions can be drawn for the network losses, which are increased in the proposed control framework, especially, during high generation periods, as shown in Fig. 4g and Table IV.

## V. CONCLUSIONS

In this paper, a new control framework is proposed that facilitates the VI provision in unbalanced, grid-connected distribution grids. This is attained by enhancing the mathematical formulation of a conventional optimal power flow formulation with additional operational constraints that model the dynamic behavior of CIRESs and distribution grids during a frequency event. Time-domain and time-series simulations

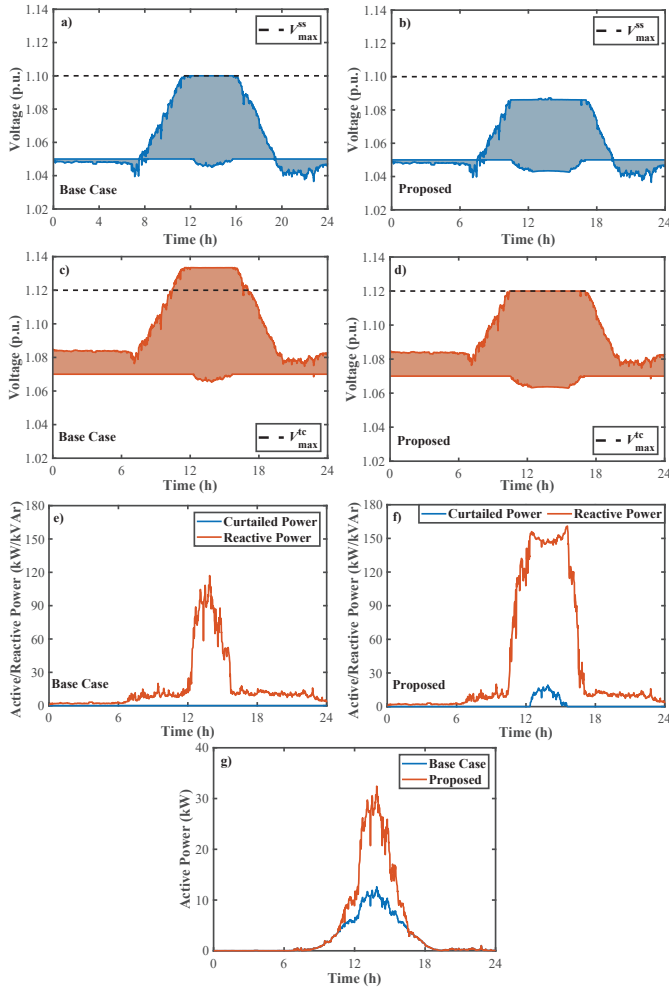


Fig. 4. Daily profiles. a), b) Variation of network voltages (shaded area) under steady-state conditions in the base case scenario and proposed method, respectively; c), d) the corresponding variation of network voltages (shaded area) under transient conditions; e), f) the corresponding overall curtailed power and reactive power use of PVs, and g) network active power losses.

on the IEEE European LV Test Feeder revealed the superiority of the proposed control framework against the base case scenario in terms of keeping the network voltages within permissible limits and avoiding CIRES tripping, at the expense of increased curtailment and reactive power usage.

Future work will be carried out to determine, from both technical and economic perspectives, the best trade-off between VI contribution from CIRESs and amount of curtailed power and/or reactive power needed to maintain the network voltages within the permissible limits under both steady-state and transient conditions. Moreover, the proposed concept will be assessed by adopting a distributed control architecture.

## REFERENCES

- [1] Z. Liu *et al.*, "A lagrange-multiplier-based reliability assessment for power systems considering topology and injection uncertainties," *IEEE Trans. Power Syst.*, vol. 39, no. 1, pp. 1178–1189, 2024.
- [2] D. Lekshmi J, Z. H. Rather, and B. C. Pal, "Online estimation of disturbance size and frequency nadir prediction in renewable energy integrated power systems," *IEEE Trans. Power Syst.*, vol. 39, no. 1, pp. 1126–1137, 2024.
- [3] Q.-C. Zhong and G. Weiss, "Synchronverters: Inverters that mimic synchronous generators," *IEEE Trans. Ind. Electron.*, vol. 58, no. 4, pp. 1259–1267, 2011.
- [4] S. Sproul, S. Cherevatskiy, and Klingenberg. Grid forming energy storage: Provides virtual inertia, interconnects renewables and unlocks revenue. Accessed on 2024-02-29. [Online]. Available: <https://www.electranet.com.au/wp-content/uploads/2021/01/Grid-Forming-Energy-Storage-Webinar-ESCRI-SA-July-2020.pdf>
- [5] S. Luo, W. Chen, X. Li, and Z. Hao, "A new virtual inertia strategy for Andronov–Hopf oscillator based grid-forming inverters," *IEEE J. Emerg. Sel. Topics Power Electron.*, pp. 1–1, article in press.
- [6] J. Fang, P. Lin, H. Li, Y. Yang, and Y. Tang, "An improved virtual inertia control for three-phase voltage source converters connected to a weak grid," *IEEE Trans. Power Electron.*, vol. 34, no. 9, pp. 8660–8670, 2019.
- [7] D. A. Aragon, E. Unamuno, A. G. de Muro, S. Ceballos, and J. A. Barrena, "Second-order filter-based inertia emulation (SOFIE) for low inertia power systems," *IEEE Trans. Power Del.*, vol. 39, no. 1, pp. 530–541, 2024.
- [8] M. Li, W. Huang, N. Tai, L. Yang, D. Duan, and Z. Ma, "A dual-adaptivity inertia control strategy for virtual synchronous generator," *IEEE Trans. Power Syst.*, vol. 35, no. 1, pp. 594–604, 2020.
- [9] F. Perez, G. Damm, C. M. Verrelli, and P. F. Ribeiro, "Adaptive virtual inertia control for stable microgrid operation including ancillary services support," *IEEE Trans. Control Syst. Technol.*, vol. 31, no. 4, pp. 1552–1564, 2023.
- [10] G. C. Kryonidis, K.-N. D. Malamaki, J. M. Mauricio, and C. S. Demoulias, "A new perspective on the synchronverter model," *Int. J. Electr. Power Energy Syst.*, vol. 140, 2022.
- [11] M. Ebrahimi, S. A. Khajehodini, and M. Karimi-Ghartemani, "An improved damping method for virtual synchronous machines," *IEEE Trans. Sustain. Energy*, vol. 10, no. 3, pp. 1491–1500, 2019.
- [12] C. Li, Y. Yang, Y. Cao, A. Aleshina, J. Xu, and F. Blaabjerg, "Grid inertia and damping support enabled by proposed virtual inductance control for grid-forming virtual synchronous generator," *IEEE Trans. Power Electron.*, vol. 38, no. 1, pp. 294–303, 2023.
- [13] M. Yang, Y. Wang, S. Chen, X. Xiao, and Y. Li, "Comparative studies on damping control strategies for virtual synchronous generators," *IEEE Trans. Power Del.*, article in press.
- [14] A. E. Leon and J. M. Mauricio, "Virtual synchronous generator design to improve frequency support of converter-interfaced systems," *IEEE Trans. Energy Convers.*, article in press.
- [15] W. Bao, Q. Wu, L. Ding, S. Huang, and V. Terzija, "A hierarchical inertial control scheme for multiple wind farms with BESSs based on ADMM," *IEEE Trans. Sustain. Energy*, vol. 12, no. 2, pp. 751–760, 2019.
- [16] M. H. Fini, M. E. H. Golshan, J. R. Mart, and A. Ketabi, "Determining the required frequency control reserve and capacity and location of synchronous and virtual inertial resources," *IEEE Trans. Sustain. Energy*, vol. 14, no. 1, pp. 27–38, 2022.
- [17] Z. Zhang, E. Du, F. Teng, N. Zhang, and C. Kang, "Modeling frequency dynamics in unit commitment with a high share of renewable energy," *IEEE Trans. Power Syst.*, vol. 35, no. 6, pp. 4383–4395, 2019.
- [18] Y. Yuan, Y. Zhang, J. Wang, Z. Liu, and Z. Chen, "Enhanced frequency-constrained unit commitment considering variable-droop frequency control from converter-based generator," *IEEE Trans. Power Syst.*, vol. 38, no. 2, pp. 1094–1110, 2023.
- [19] "IEEE Standard for Interconnection and Interoperability of Distributed Energy Resources With Associated Electric Power Systems Interfaces," *IEEE Std 1547a-2020 (Amendment of IEEE Std 1547-2018)*, 2020.
- [20] J. M. Mauricio, J. C. Olives-Camps, J. M. Maza-Ortega, and A. Gómez-Expósito, "Integrated simulation of electromechanical and thermal dynamics of voltage source converters," *Int. J. Electr. Power & Energy Syst.*, vol. 155, p. 109672, 2024.
- [21] IEEE PES Analytic Methods for Power Systems Technical Committee and Distribution System Analysis Subcommittee Test Feeder Working Group. [Online]. Available: <https://cmte.ieee.org/pes-testfeeders/>
- [22] G. C. Kryonidis *et al.*, "Distributed reactive power control scheme for the voltage regulation of unbalanced LV grids," *IEEE Trans. Sustain. Energy*, vol. 12, no. 2, pp. 1301–1310, 2021.
- [23] GAMS Development Corporation, "General Algebraic Modeling System (GAMS) Release 24.8." [Online]. Available: <https://www.gams.com>
- [24] Altair Engineering, "Powersim Professional 2022.2.0.17." [Online]. Available: <https://altair.com/psim>